https://doi.org/10.5194/egusphere-2026-2637
Preprint. Discussion started: 20 May 2026

Unraveling Spatial Dependencies in Landslide Susceptibility using Directed Acyclic Graphs

Qingkai Meng[a, *], Yong Dai[a, b], Filippo Catani[c], Shilong Chen[a, d], Qiuhui Wang[a, b], Qing Li[a], Ying Peng[e], Han Wu[a], Ying Meng[a, b]

[a]State Key Laboratory of Mountain Hazards and Engineering Resilience, Institute of Mountain Hazards and Environment, Chinese Academy of Sciences, Chengdu 610213, China

[b]School of Civil Engineering and Water Resources, Laboratory of Ecological Protection and High Quality Development in the Upper Yellow River, Qinghai University, Xining 810016, China

[c] Machine Intelligence and Slope Stability Laboratory, Department of Geosciences, University of Padua, Padua, 35129, Italy

[d] College of Geophysics, Chengdu University of Technology, Chengdu 610059, China

[e] The College of Nuclear Technology and Automation Engineering, Chengdu University of Technology, Chengdu 610059, China

**Correspondence: Qingkai Meng (mengqingkai@imde.ac.cn)*

Abstract. Data-driven methods for landslide susceptibility assessment (LSA) often suffer from spurious correlations and “black-box” opacity, failing to capture the spatial dependency processes underlying landslide development. To address these limitations, we propose a directed acyclic graph (DAG)-informed interpretable framework by integrating structure-learning algorithms and graph attention models. This approach enables the identification of spatial dependency pathways and quantifies the propagation magnitudes (weights of connected links) of landslide conditioning factors. We applied this framework to the Ili River Basin, Xinjiang, China. A total of 14 robust spatial dependency chains were identified, and the dominant susceptibility-related chains were categorized into four types: (1) Elevation–climate-driven pathways (Elevation → Precipitation → NDWI → Landslide; Elevation → Precipitation → Temperature → Snow Depth → NDWI → Landslide); (2) Tectonic-controlled pathways (Distance to faults → PGA → Landslide); (3) Topographic dominated pathways (Slope → Curvature → Landslide); and (4) Hydrological driven pathways (Distance to rivers → NDWI → Landslide). Using a novel importance-weighted decoupling method, we generated pathway-specific susceptibility maps. These four chains account for 18.32%, 15.74%, 17.67%, and 16.76% of the high-susceptibility areas, respectively. These areas are predominantly clustered in mid–high mountainous, high-intensity seismic, and weakened lithological belt regions. Our proposed framework advances LSA from statistical prediction to dependency-informed explanation, providing decision-makers with a scientific basis for interpreting susceptibility variations across different spatial and environmental settings.

Keywords: explainable artificial intelligence; spatial dependency; landslide susceptibility assessment; directed acyclic graph; graph attention network; the Ili River Basin.

Graphical Abstract

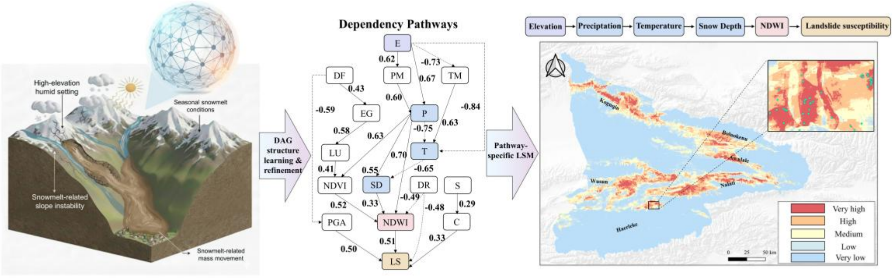

1 Introduction

A landslide is the gravity-driven downslope movement of rock, debris, or earth, occurring in both sub-aerial and subaqueous environments (Cruden and Varnes, 1996). Landslide Susceptibility Assessment (LSA) provides the scientific foundation for hazard mitigation, land-use planning, and infrastructure site selection by evaluating landslide-prone zones at the regional scale (Guzzetti et al., 2012). At the regional scale, landslide susceptibility patterns are influenced by a complex, non-linear coupling of environmental factors, including precipitation conditions, topographic relief, geological lithology, and tectonic activity (Alvioli et al., 2024).

Given the complexity of landslide-environment relationships, data-driven approaches—particularly Machine Learning (ML) and Deep Learning (DL)—have superseded traditional heuristic and statistical methods as the dominant paradigm in LSA (Li et al., 2024). By mining latent relationships between environmental factors and historical landslide inventories, state-of-the-art models, such as TabPFN, Transformer-based models, and hybrid ensemble frameworks, have achieved superior predictive accuracy (Nocentini et al., 2024; Caleca et al., 2025; Hussain et al., 2025; Lee et al., 2025). However, the inherent “black-box” characteristics of these approaches often limit the interpretability of individual

https://doi.org/10.5194/egusphere-2026-2637
Preprint. Discussion started: 20 May 2026

feature contributions to landslide susceptibility, thereby undermining their credibility in practical disaster management and engineering decision-making contexts (Camps-Valls et al., 2025).

To address this transparency gap, Explainable Artificial Intelligence (XAI) has been introduced to construct explanatory models for classes of real-world phenomena that can be communicated to humans (Adadi and Berrada, 2018). XAI primarily encompasses three categories: data explainability, model explainability, and post-hoc explainability (Ali et al., 2023). Post-hoc interpretation methods, such as SHAP and LIME, are widely adopted to rank the contributions of landslide conditioning factors in recent years (Pradhan et al., 2023; Utthasini et al., 2025; Bhattarai et al., 2026). Nevertheless, a critical limitation persists: these methods primarily explain statistical associations rather than directional dependencies, which may lead to "spurious correlation" fallacies (Youssef et al., 2023). For instance, a model might attribute low landslide probability to "low vegetation coverage" while overlooking the confounding variable of "urbanization" (where concrete surfaces reduce vegetation but also reduce slope instability) (Matougui et al., 2025). Similarly, gentle slopes might be identified as safe zones without accounting for the cascading effects of irrigation-induced saturation (Xu et al., 2022). Such post-hoc explainability fails to distinguish spatial dependency pathways, rendering them insufficient for understanding the true etiological chains of landslides (Steger et al., 2021).

In contrast to correlation-based XAI, Directed Acyclic Graphs (DAGs) network offers a way to represent directional relationships in complex systems, which consist of a set of nodes and directed links (Digitale et al., 2022; Gao et al., 2025). By encoding environmental variables as nodes and directed influences as edges, DAGs can theoretically reveal the structures of landslide development, implying a cognitive map of where and how the environmental factors impact the landslides system (Chen et al., 2021; Zhou et al., 2024). Unfortunately, such DAG inference methods are still only known within a small community machine learning developer, limited attempts have been made to the application of LSA.

Unlike previous studies that focus on slope-scale physical process causality, which is difficult to constrain in large-area assessments due to the limited availability of detailed physical parameters, our DAG-informed neural network is designed to characterize regional-scale directed dependencies among multiple environmental factors. In this way, it provides a model explainability to unify knowledge discovery and high-accuracy susceptibility prediction. Specifically, the framework comprises three components: (1) constructing a knowledge-guided directed dependency structure by optimizing multiple structure-learning algorithms to reduce spurious links and improve geological interpretability; (2)

https://doi.org/10.5194/egusphere-2026-2637
Preprint. Discussion started: 20 May 2026

extracting dominant dependency pathways from the DAG structure and analyzing their spatial associations with landslide susceptibility; and (3) performing DAG-informed susceptibility prediction by jointly examining the attribution characteristics of the global landslide susceptibility map and the importance of pathway-specific patterns. Overall, our research offers an interpretable methodological perspective for developing more explainable and differentiated prevention and preparedness strategies for geological hazards, thereby providing decision-makers with a more transparent tool for understanding susceptibility distributions associated with different landslide-forming settings.

2 Study area and Datasets

2.1 Study area

The Ili River Basin in Xinjiang, China, located in the northwest of the Xinjiang Uygur Autonomous Region, bordering Kazakhstan to the west. The basin is surrounded by the northern branch of the Tianshan Mountains, exhibiting a distinctive geomorphological pattern of three mountains ranges encircling two valleys and a central basin (Xu et al., 2015; Ailhamu., 2022). Twelve active fault zones, including the northern margin fault of the Ili Basin, the southern slope faults of the Awulale Mountains, the Kekeboh River faults, and the Nalati faults, traverse the region from north to south (Zhang et al., 2025). The Ili River, fed by major tributaries—the Tekes, Gongnaisi, and Kashi Rivers—dominates surface runoff. Climatically, the basin experiences temperatures ranging from −17.5°C to 26.3°C and annual precipitation of 200–550 mm (Chen et al., 2025). Its west-wide, east-narrow topography, coupled with prevalent rainfall and seismic activity, renders the basin an exemplary case for landslide susceptibility assessment. (Fig. 1).

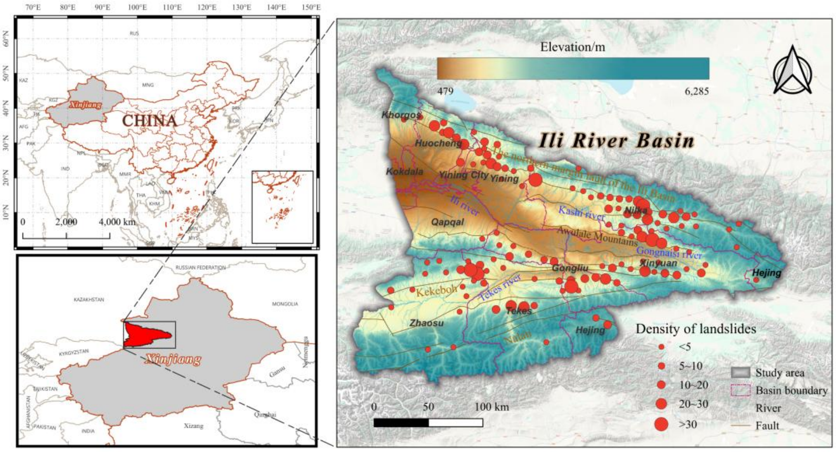

Figure 1: **The location of the Ili River Basin and the distribution of landslides**

2.2 Landslide inventory data

The landslide inventory serves as the foundational ground truth for susceptibility modeling (Castro-Venegas et al., 2025). In this study, a comprehensive inventory containing 1,198 landslides was constructed for the Ili River Basin through a synergy of field investigations and visual interpretation of high-resolution optical remote sensing imagery (Fig. 1). The identified landslides are predominantly small- to medium-scale shallow translational slides developed in Quaternary loess. Spatially, these events are clustered in the mid-to-high mountainous zones and fluvial terraces along river valleys.

2.3 Predisposing environmental factors

Based on the geo-environmental characteristics of the Ili River Basin and data availability, 15 conditioning factors were selected and categorized into four groups for LSA modeling (Table 1; Fig. 2).

(1) Topographic Factors: Three factors were derived from the DEM: elevation, slope, and curvature. Landslide density analysis reveals that majority landslides are concentrated in elevations of 1,000–2,000 m and slopes of 8°–40°. Slopes with curvature values between −0.04 and 0.04 m^{-1} are more prone to landslides (Fig. 2a-2c).

(2) Geological and Tectonics Factors: These parts include Lithology, Distance to Faults, and PGA. The Lithology layer was reclassified into five engineering geological units (Fig. 2d), with Quaternary loess and soft sedimentary rocks exhibiting the highest failure frequency. Proximity to faults (<1.6 km) and

high seismic intensity zones (PGA ≥ 0.3 g) show significantly elevated landslide densities, reflecting the impact of tectonic activity (Fig. 2e, 2f).

(3) Hydrological Factors: This category includes distance to rivers and NDWI. Landslides exhibit a dense distribution within 2,400 m of river channels such as the Ili, Tekes, and Kashi Rivers (Fig. 2g). NDWI ranges from 0.15–0.45, indicating a moderate to high level of soil moisture content and shallow groundwater, which contributes to the reduction of soil shear strength and promotes slope instability (Rahimikhameneh et al., 2025) (Fig. 2h).

(4) Climatic and Environmental Factors: This group comprises land use, NDVI, annual/monthly mean precipitation, snow depth and annual/monthly mean temperature (Fig. 2i-2o). Landslides predominantly occur in bare land and shrub areas with moderate vegetation cover (NDVI: 0.2–0.6). Temperature variables characterize the freeze-thaw cycles; regions with annual mean temperatures of −3 to 6 °C are identified as high-prone zones due to the frost weathering effect on rock and soil masses. Precipitation variables (200–350 mm/year) and snow depth (0.05–0.4 m) highlight the specific role of rainfall-infiltration and snowmelt in destabilizing loess slopes, particularly in the Koguqin and Nalati Mountains. All spatial datasets were resampled to a unified resolution of 30 m × 30 m to ensure compatibility and processed in ArcGIS 10.2.

Table 1. Data Sources of Influencing Factors

Category	Evaluation Factor (Abbreviation)	Data Sources
Topographic Factors	Elevation(**E**), slope(**S**), curvature(**C**)	https://www.gscloud.cn/
Geological and Tectonics Factors	Engineering geological lithology (**EG**), distance to faults (**DF**), peak ground acceleration (**PGA**)	**EG, DF:** Natural Resources Archives of the Xinjiang Uygur Autonomous Region (http://zrzyt.xinjiang.gov.cn) **PGA:** The fifth national risk census data.
Hydrological Factors	Distance to river (**DR**), Normalized Difference Water Index (**NDWI**)	**DR:** https://www.gscloud.cn/ **NDWI:** https://developers.google.com/earth-engine/datasets/catalog/
Climatic and Environmental Factors	Normalized Difference Vegetation Index (**NDVI**), land use type (**LU**), annual mean precipitation(**P**), monthly mean precipitation (**PM**), annual mean	**NDVI:** https://developers.google.com/earth-engine/datasets/catalog/ **LU:** https://livingatlas.arcgis.com/landcover/ **P, PM, T, TM, SD:**

	temperature(**T**), monthly mean temperature (**TM**), annual average snow depth (**SD**)	https://climate.copernicus.eu/climate-reanalysis

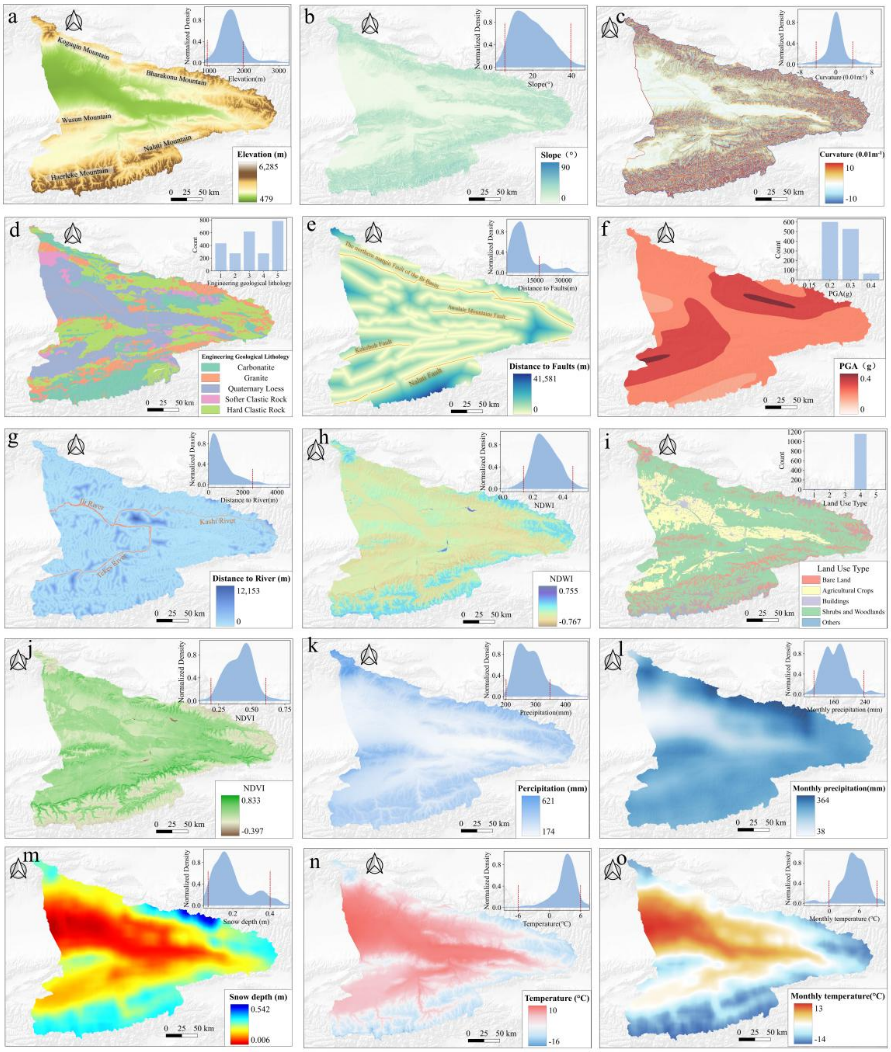

Figure 2: Spatial distribution mapping of predisposing factors. Notably, the top right corner represents the data density distribution, where red line represent 80% of the total area

3 Methodologies

This study establishes an Explainable DAG-guided Neural Network (EDNN) framework for Landslide Susceptibility Assessment (LSA). As illustrated in Fig. 3, the framework comprises three modules: (1)

DAG structure-learning algorithms, (2) Knowledge-Guided Refinement and Weight Learning, and (3) pathway-based landslide susceptibility assessment. To characterize the complex interplay network among environmental factors, we first construct a fully connected undirected graph. Landslide and non-landslide samples are extracted, where landslide occurrence (0, 1) and 15 conditioning factors are defined as independent nodes. We optimize different algorithms to infer the initial directed graph structure (I-DAG), and the direction of the connected link represents a modeled directional dependency. Expert-guided knowledge refinement is then adopted to ensure geological and logical interpretability (E-DAG). Finally, graph attention was employed to updated all nodes and weights of connected links to generate the final structure(F-DAG).

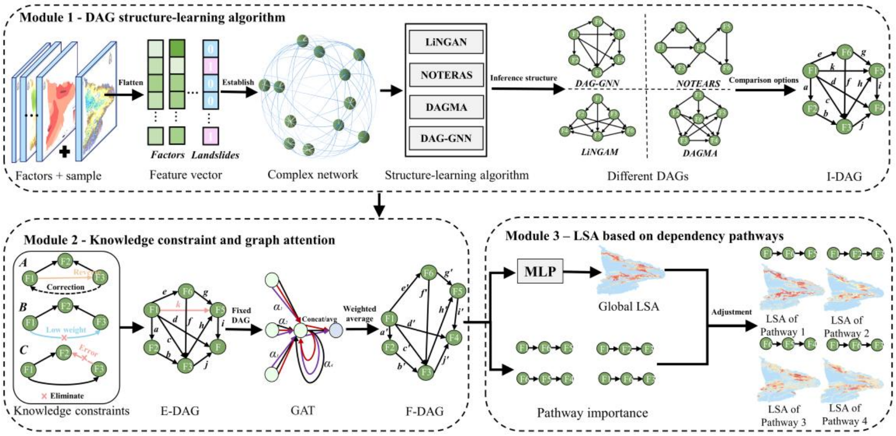

Figure 3: EDNN framework. I-DAG, E-DAG, and F-DAG represent the initial DAG from structure learning, the refined DAG by expert knowledge, and the final DAG with updated weights, respectively. F1-F6 are illustrative predisposing factors, and lowercase letters represent the weights of connected links

3.1 Module 1: DAG structure-learning algorithm selection

To infer the directed graph structure from observational data, we integrated and compared four state-of-the-art algorithms: LiNGAM (Shimizu et al., 2006), DAGMA (Bello et al., 2022), NOTEARS (Zheng et al., 2018), and DAG-GNN (Yu et al., 2019). Different algorithms formulate graph structures under their respective assumptions. Among them, DAG-GNN employs an Encoder-Decoder architecture. The encoder, implemented as a Multi-Layer Perceptron (MLP), incorporates the adjacency matrix transpose to map input data into a potential representation. The decoder reconstructs the data distribution and minimizes the discrepancy between predicted and original distributions with another matrix inversion

MLP (Fig. 4). Gradient descent optimizes the Encoder-Decoder, converging to a DAG by balancing reconstruction error and graph structure constraint loss, the equation is shown as:

$$\mathcal{L} = \alpha \cdot \| X - \hat{X} \|_F^2 + \mathrm{tr}\left((\mathbf{I} - \mathbf{A}^T)^{-1} \right) - n \tag{1}$$

Here, α is the coefficient, set to 0.7, X denotes the original distribution, and $\hat{X}$ denotes the predicted distribution. $\mathrm{tr}(\cdot)$ represents the trace of a matrix, and n is the number of nodes, set to 16. **I** is the identity matrix, **A** is the adjacency matrix, and $\mathbf{A}^{\mathrm{T}}$ is its transpose (Yu et al., 2019).

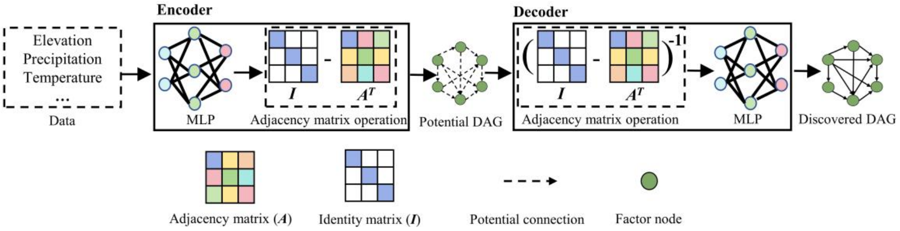

Figure 4: The Encoder-Decoder structure of the DAG-GNN model. The adjacency matrix is another form of the DAG, where the vertical axis represents upstream nodes and the horizontal axis represents downstream nodes, with the matrix elements representing the magnitude of edge weights. (Revised from Yu et al., 2019)

Given the inconsistency of edge weights across different structure-learning algorithms, we apply the hyperbolic tangent function, tanh (0.5x) to normalize the weights of connected links, and make them more suitable for landslide susceptibility analysis (LSA).

$$w_i = \tanh(0.5x) = \frac{e^{0.5x} - e^{-0.5x}}{e^{0.5x} + e^{-0.5x}} \tag{2}$$

In this equation, e is a natural constant, and x is a weight (Liu and Di, 2021).

To explain a specific pathway contribution, we establish the geometric mean of pathway weights following the study of Pearl (2000):

$$\text{Importance} = \left| \prod_{i=1}^{n} w_i \right|^{\frac{1}{n}} \tag{3}$$

Where n denotes the number of connected links in the pathway.

3.2 Module2: Knowledge constraint and graph attention

Considering erroneous connections from the initial DAG generated by structure learning, this study enforces physical plausibility through three constraint strategies: (1) End node constraint. All connections must point towards the "Landslide" end node; (2) Unreliable connection constraint. Weak connections with smoothed weights below 0.30 are pruned. This removes noisy or unreliable connections; (3) Logical constraints. Edges with incorrect pathway directions (e.g., temperature → elevation) or implausible relationships (e.g., precipitation → distance to fault) are removed based on expert knowledge. This detail can be shown in Fig. 3.

Since expert knowledge may affect edge weights, we employ Graph Attention Networks (GAT) (Veličković et al., 2017) to relearn the dependency strengths. GAT computes attention coefficients between a central node and its neighbors, followed by directed weighted aggregation, which is used to update weights locally and globally at the grid-cell level using the LeakyReLU and Softmax functions:

$$\alpha_{ij} = \mathrm{Softmax}_j\left(\mathrm{LeakyReLU}\left(\mathbf{a}^{\top}\left[\mathbf{Wh}_i \| \mathbf{Wh}_j\right]\right)\right) \tag{4}$$

Here, α_{ij} are attention coefficients used to measure the importance of a node, || represents the concatenation of attention heads, LeakyReLU(·) and Softmax(·) are activation functions, $\mathbf{h}_i$ and $\mathbf{h}_j$ represent node features, **W** is the shared transformation matrix, and **a** is a learnable vector (Velickovic et al., 2017).

For multi-head attention, the attention coefficients from k heads are concatenated or averaged, and the updated node representation is:

$$h_i' = \|_{m=1}^{k} \sigma\Big(\sum_j \alpha_{ij}^{(m)} \mathbf{W}^{(m)} h_j\Big) \tag{5}$$

Where σ is an activation function, and denotes concatenation of k attention heads (Veličković et al., 2017). The GAT refines the edge weights in the DAG by assigning higher attention to more relevant connections within each grid cell, improving the representation of local structured relationships. The learned DAG's structural and weight information are encoded into a feature vector, then input into a Multi-Layer Perceptron (MLP) to predict global landslide probabilities.

3.3 Module 3: Landslide susceptibility assessment based on dependency pathways

This study proposes an importance-weighted framework for estimating landslide susceptibility probability (LSP) under pathway-specific control. The framework integrates the global landslide susceptibility probability, pathway importance, and the Spearman correlation coefficient (Zhou and Xing, 2025), which quantifies the spatial consistency between the global susceptibility pattern and individual dependency pathways. A negative Spearman coefficient indicates spatial inconsistency and leads to a suppressive effect on LSP, whereas vice versa. The landslide susceptibility probability controlled by a single pathway (LSP-chain) is formulated as follows:

$$\mathrm{LSP}_{\mathrm{chain}} = \sigma\left(\alpha\,\mathrm{logit}(\mathrm{LSP}) + (1-\alpha)\,\mathrm{sgn}(r)\,|r|^{\gamma} I_{\mathrm{chain}}\right) \tag{6}$$

Here, α denotes the trust coefficient, which is set to 0.2, and γ represents the modulation exponent, with a value of 0.5. The functions σ(·) and sgn(·) denote the Sigmoid function and the sign function, respectively (Fig. 5).

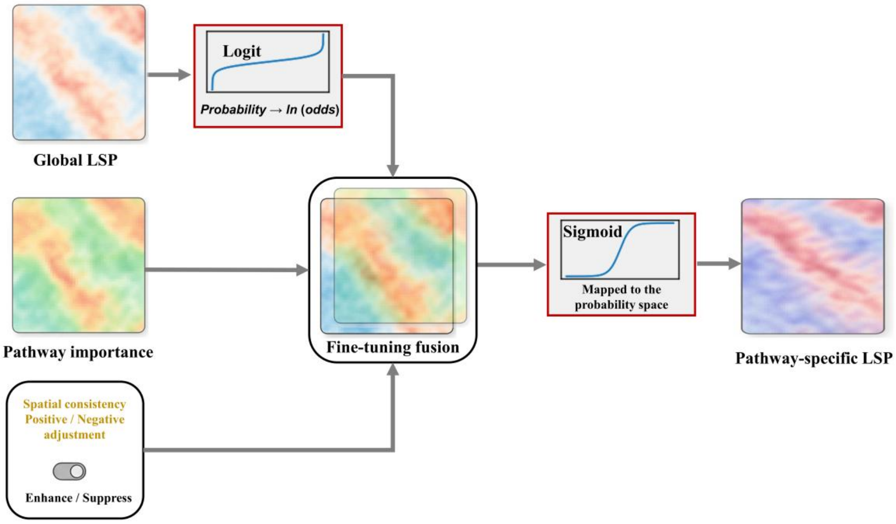

Figure 5: Landslide susceptibility calculation process based on dependency pathways

4 Results

4.1 Discovery F-DAG

The dependency structures inferred by the four algorithms (LiNGAM, DAGMA, NOTEARS, and DAG-GNN) exhibited significant differences in structural plausibility (Fig. 6; Supplementary-Fig. S1; Table 2). The LiNGAM, DAGMA, and NOTEARS algorithms captured 32, 29, and 30 edges, respectively, at the initial stage. However, these discovered edges demonstrated high error rates in complex geological contexts. After applying knowledge refinement, LiNGAM removed 11 erroneous edges (including 5 low-weight unreliable connections and 6 elevation-dependent implausible connections) (Supplementary-Fig. S1f). Similarly, NOTEARS and DAGMA removed 7 and 10 erroneous edges and reversed 3 and 2 incorrectly directed connections, respectively. Among the spurious connections, six were associated with climatic and tectonic factors (Supplementary-Fig. S1h). These results indicate that the three algorithms share common limitations: they either rely on linear/parametric assumptions or lack effective modeling capability for complex spatial relationships, making their inferred structures highly susceptible to data noise and statistical spurious correlations, and thus unable to automatically yield concise dependency structures consistent with physical mechanisms (Zhao and Jia, 2025).

In contrast, DAG-GNN demonstrated superior robustness and structural consistency. It identified 30 initial connections, of which only 7 required modifications (2 reversed, 3 unreliable, and 2 implausible) under expert validation, which is substantially fewer than the other three algorithms (Supplementary-Fig. S1e). Across most evaluation metrics, DAG-GNN consistently achieved the best performance, obtaining higher Accuracy, AUC, F1-score, and Recall values (Table 2). The overall performance ranking was DAG-GNN > DAGMA > NOTEARS > LiNGAM. This advantage can be attributed to the fact that DAG-GNN adopts a variational graph autoencoder (VGAE) framework based on graph neural networks, which is capable of directly modeling complex nonlinear dependencies and potential latent variables (Yu et al., 2019). Ultimately, 23 physically consistent dependency connections were retained to form the Final DAG (F-DAG), namely: E → PM, E → P, E → TM, E → T, DF → PGA, DF → EG, PM → P, TM → T, EG → LU, P → NDVI, P → SD, P → NDWI, P → T, LU → NDVI, T → SD, NDVI → NDWI, SD → NDWI, DR → NDWI, DR → LS, S → C, PGA → LS, NDWI → LS, and C → LS.

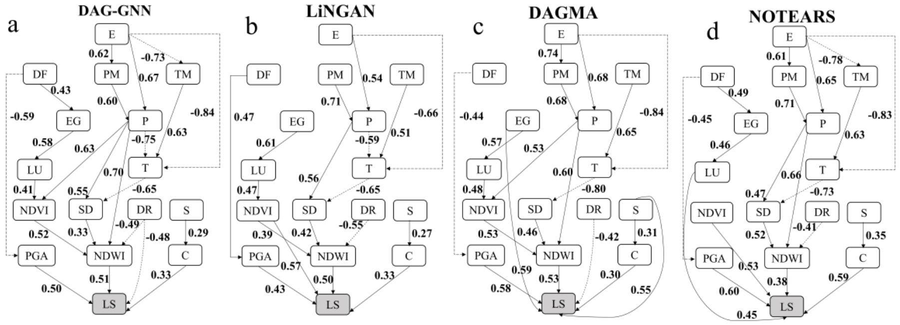

Figure 6: The final directed acyclic graph (F-DAG) discovered using four dependency structure learning algorithms. Solid and dashed lines indicate positive and negative contribution, respectively

Table 2 The result indicators of dependency structure learning algorithms

Algorithm	Original connection	After constraint	Accuracy	Precision	Recall	F1-Score	AUC
DAG-GNN	30	23	0.90	0.91	0.93	0.92	0.89
LiNGAM	32	18	0.84	0.85	0.83	0.84	0.87
DAGMA	29	20	0.88	0.89	0.87	0.88	0.87

NOTEARS	30	20	0.84	0.86	0.94	0.90	0.85

4.2 Dependency Pathways Discovery

Based on the F-DAG structure characterizing spatial relationships, a total of 14 dominant dependency pathways were extracted from optimal DAG-GNN (Table 3). Each dependency pathways is the set of nodes and links that connect a starting node with an end node. The (+)/ (−) symbols on the connections indicate positive and negative contributions, respectively. The weight is obtained from the Pathway Importance (see section 3.2) to reflect the influence of these pathways. We categorized these 14 dominant dependency pathways in to four types via starting node:

Elevation-driven dependency pathways (Chains 1–10, Table 3): Elevation acts as the fundamental predisposing factor, exerting influence through a coupled topography–climate–hydrology progress. Among them, Chain 7 (E → P → NDWI → LS) exhibits the highest importance (0.62), revealing a classic orographic precipitation effect, here high-elevation relief amplifies rainfall, thereby increasing surface soil saturation (NDWI). Chains involving temperature and snow depth (e.g., Chains 8–10, Table 3) also show high importance (~0.55). This reflects the contribution of snowmelt and freeze–thaw cycles in alpine regions of Ili Basin. Overall, elevation forms fundamental the landslide formative background (Importance 0.50–0.62, Chains 1–6, Table 3). Under the synergistic effect of high precipitation and low temperature, the important contribution of these chains dominated the central and northern Ili River Basin (e.g., Koguqin and Boluokenu Mountains) (Fig. 7a–b).

Tectonic-controlled dependency pathways (Chains 11 and 12, Table 3): Chain 11 (DF → PGA → LS) plays a dominant role (importance = 0.54). It identifies a direct pathway where fault proximity amplifies ground motion (PGA), serving as the key dynamic driver for slope failure. Chain 12 (DF →EG → LU → NDVI → NDWI → LS)(Importance = 0.49) highlights an indirect mechanism by involving more nodes. Fault zones alter the Engineering Geological (EG) properties and surface cover (LU/NDVI), which in turn creates preferential flow paths for infiltration (modifying NDWI), thereby forming a complex tectonic-geological–hydrological coupling process. This group of dependency pathways reflect active faults control the spatial distribution of landslide susceptibility by PGA and weakening the rock–soil structure. Spatially, these effects are mainly distributed along the Kokbo River Fault, the southern margin fault of the Zhaosu Basin, the Nalati Fault, and the northern margin fault of the Ili Basin, controlling the susceptibility distribution through seismic dynamics (Fig. 7c).

Hydrological interaction dependency pathway (Chain 13, Table 3): This pathways (DR → NDWI → LS) reveals the spatial constraint mechanism of river systems on landslides. Distance to River (DR) regulates slope stability by controlling the local hydrological environment. Proximity to river channels facilitates groundwater level uplift and surface runoff convergence, leading to increased soil moisture saturation (NDWI) and a subsequent reduction in shear strength. Spatially, this dependency pathway exhibits clustered distributions, mainly concentrated in river valley areas (Fig. 7d).

Topographic geometry dependency pathway (Chain 14, Table 3): This pathway (S → C → LS) quantifies the fundamental influence of micro-topography. With a relatively lower importance value of 0.31, it suggests that Slope's impact on Curvature in landslide development is insufficient in the study area. Instead, the function of these pathways can be amplified when with external conditions (e.g., rainfall infiltration or seismic loading). The effects are locally pronounced in the steep terrains of the Koguqin and Wusun Mountains (Fig. 7e).

Table 3 Regional dependency pathways. * indicates a dominant causal chain with high importance value; $^{(+)}$ and $^{(-)}$ indicate positive and negative effects

Type	Initial node	Number	Primary dependency pathways	Importance
Elevation-driven	Elevation (E)	1	$\mathrm{E} \rightarrow^{(+)} \mathrm{PM} \rightarrow^{(+)} \mathrm{P} \rightarrow^{(+)} \mathrm{NDVI} \rightarrow^{(+)} \mathrm{NDWI} \rightarrow^{(+)} \mathrm{LS}$	0.57
		2	$\mathrm{E} \rightarrow^{(+)} \mathrm{PM} \rightarrow^{(+)} \mathrm{P} \rightarrow^{(+)} \mathrm{SD} \rightarrow^{(+)} \mathrm{NDWI} \rightarrow^{(+)} \mathrm{LS}$	0.51
		3	$\mathrm{E} \rightarrow^{(+)} \mathrm{PM} \rightarrow^{(+)} \mathrm{P} \rightarrow^{(+)} \mathrm{NDWI} \rightarrow^{(+)} \mathrm{LS}$	0.60
		4	$\mathrm{E} \rightarrow^{(+)} \mathrm{PM} \rightarrow^{(+)} \mathrm{P} \rightarrow^{(-)} \mathrm{T} \rightarrow^{(-)} \mathrm{SD} \rightarrow^{(+)} \mathrm{NDWI} \rightarrow^{(+)} \mathrm{LS}$	0.56
		5	$\mathrm{E} \rightarrow^{(+)} \mathrm{P} \rightarrow^{(+)} \mathrm{NDVI} \rightarrow^{(+)} \mathrm{NDWI} \rightarrow^{(+)} \mathrm{LS}$	0.58
		6	$\mathrm{E} \rightarrow^{(+)} \mathrm{P} \rightarrow^{(+)} \mathrm{SD} \rightarrow^{(+)} \mathrm{NDWI} \rightarrow^{(+)} \mathrm{LS}$	0.50
		7*	$\mathrm{E} \rightarrow^{(+)} \mathrm{P} \rightarrow^{(+)} \mathrm{NDWI} \rightarrow^{(+)} \mathrm{LS}$	0.62
		8*	$\mathrm{E} \rightarrow^{(+)} \mathrm{P} \rightarrow^{(-)} \mathrm{T} \rightarrow^{(-)} \mathrm{SD} \rightarrow^{(+)} \mathrm{NDWI} \rightarrow^{(+)} \mathrm{LS}$	0.56
		9	$\mathrm{E} \rightarrow^{(-)} \mathrm{TM} \rightarrow^{(+)} \mathrm{T} \rightarrow^{(-)} \mathrm{SD} \rightarrow^{(+)} \mathrm{NDWI} \rightarrow^{(+)} \mathrm{LS}$	0.55

		10	$E \to^{(-)} T \to^{(-)} SD \to^{(+)} NDWI \to^{(+)} LS$	0.55
Tectonic-controlled	Distance to Fault (DF)	11*	$DF \to^{(-)} PGA \to^{(+)} LS$	0.54
		12	$DF \to^{(+)} EG \to^{(+)} LU \to^{(+)} NDVI \to^{(+)} NDWI \to^{(+)} LS$	0.49
Hydrological erosion	Distance to River (DR)	13*	$DR \to^{(-)} NDWI \to^{(+)} LS$	0.50
Topographic geometry	Slope (S)	14*	$S \to^{(+)} C \to^{(+)} LS$	0.31

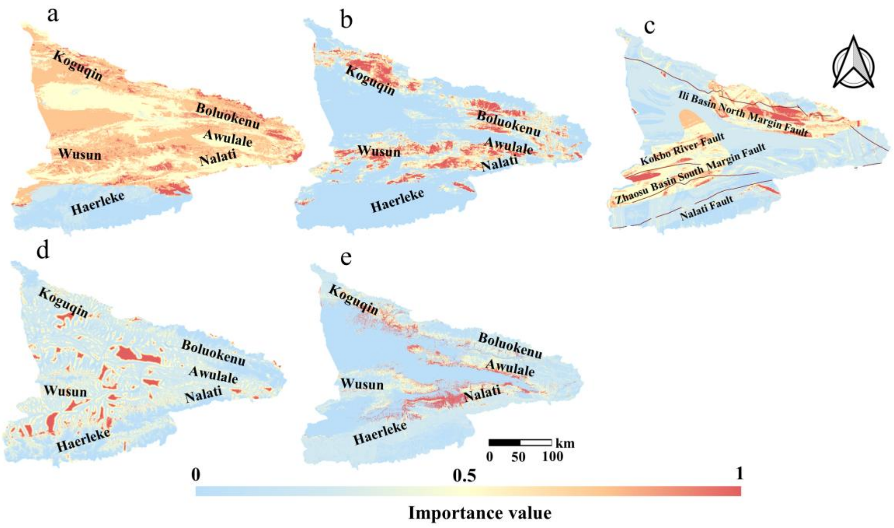

Figure 7: Spatial distribution of dependency pathway importance, representing the strength of the dependency pathway's effect across the region, where 0 indicates no effect and 1 indicates strong effect. a–e respectively represents the importance distributions of E → P → NDWI→ LS, E → P→ T → SD→ NDWI → LS, DF → PGA → LS, DR → NDWI → LS, and S → C → LS

4.3 Landslide Susceptibility Assessment（LSA）

To demonstrate the multi-scale interpretability of the proposed framework, we generated both global-level and pathway-specific -level susceptibility maps based on the learned F-DAG structure.

4.3.1 LSA at global scale

Leveraging the dependency pathways aggregated by the F-DAG, the EDNN model generated a global landslide susceptibility map. The susceptibility values were stratified into five levels—Very Low, Low, Moderate, High, and Very High—using the natural breaks classification method. Statistically, the High and Very High susceptibility zones cover 8.63% and 7.65% of the total study area, respectively, cumulatively accounting for 16.28% of the region (the total number of landslides included is 1023). Spatially, these high-risk areas are predominantly clustered in mid-to-high altitude mountainous terrain, active seismic intensity zones, Proximity to river channels and weaken lithological formations (Fig. 8). Visual inspection confirms that the predicted high-prone zones exhibit strong spatial consistency with the inventory of historical landslides, aligning with findings from previous studies (Tao et al, 2016; Dai et al, 2024).

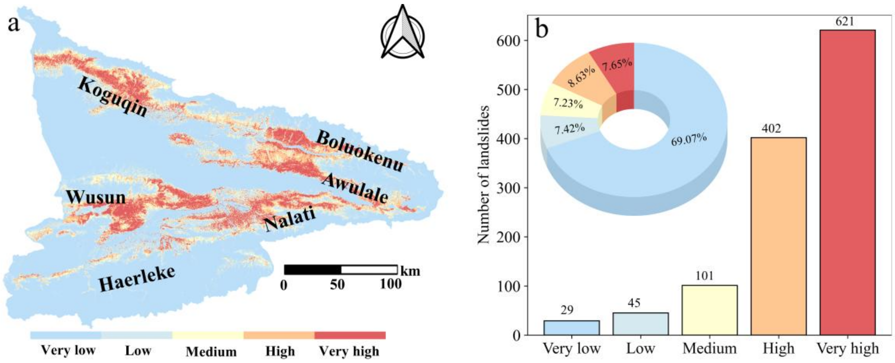

Figure 8: Global LSA results obtained using the EDNN model. (a) Spatial distribution and (b) statistical results. The bar chart and pie chart represent the number of landslides and the proportion of area within each zone, respectively

4.3.2 LSA based on different dependency pathways

To disentangle the spatial heterogeneity driven by distinct spatial dependency mechanisms, we generated pathway-specific susceptibility maps based on four representative dependency pathways (Chain 7, 8, 11, 14) selected from Table 3 (Fig. 9). These maps quantify the contribution of specific dependency pathways to the overall landslide risk.

Elevation–Precipitation Chain E →P →NDWI→LS (Chain 7): the susceptibility pattern driven by this pathway accounts for 18.32% of the study area as high-risk zones (Very High + High). Spatially, it manifests as a continuous zonal distribution oriented east–west, predominantly covering the windward slopes of the mid- to high-elevation zones in the Koguqin, Northern Boluokenu, and Nalati Mountains (Fig. 9a). This susceptibility pattern is closely associated with the mid-latitude westerlies, which transport moist air masses into the Ili River Valley from west to east (Hu et al, 2023). The interaction between the westerly airflow and the windward slopes of the mid- to high-elevation mountains enhances orographic precipitation, thereby reinforcing the Elevation–Precipitation–NDWI–LS pathway.

Elevation–Snowmelt Chain E →TM→T →SD→NDWI →LS (Chain 8): the snowmelt-driven pathway governs 15.74% landslide susceptibility area of the basin. Its landslide formative process involves winter snow accumulation followed by spring warming and melting, which enhances intensify of freeze the frozen and water supply conditions and facilitates the development of sinkholes and the propagation of cracks in the loess (Li et al., 2023). Spatially, it located to specific low-temperature alpine zones with deep snow coverage (e.g. Koguqin Mountain to Awulale Mountain, Wusun Mountain to Nalati Mountain) (Fig. 9b).

Seismic-Dynamic Chain (Chain 11): Notably, this pathway yields a notably wide high-risk footprint, accounting for 17.67% of the basin. It displays pronounced clustered distributions and belt-like patterns along main fault. Crucially, the high-susceptibility zones show closely spatial congruence with the rupture zones of the historic the 1812 Nilka Mw 8.0 earthquake and the 2003 Zhaosu Mw 6.1 earthquake (Havenstrite et al., 2015) (Fig. 9c).

Morphology-Dominated Chain (Chain 14) Controlled by local topographic geometry, this pathway influences 16.76% of the area. High-risk zones are characterized by steep gradients and complex curvature, concentrated in the rugged terrains of the northern/southern basin margins and the central Wusun Mountains (Fig. 9d). This map delineates areas where gravitational potential energy is the primary driver of instability.

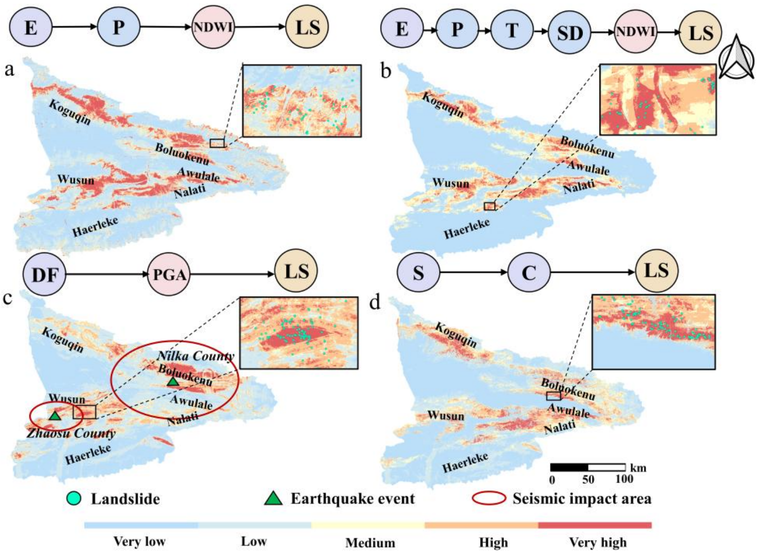

Figure 9: The landslide susceptibility map based on dependency pathways. The boxes correspond to enlarged views of typical disaster sites selected from their respective regions. Panel c shows the impact zones of two seismic events

5 Discussion

5.1 Model robustness

To evaluate the contribution of individual components of the EDNN model, module ablation experiments were conducted, and each experiment was repeated 10 times (Fig. 10). Fig. 10a reveals a significant performance degradation across all statistical metrics upon module removal, confirming the necessity of the proposed modular integration. Specifically, the "MLP only" configuration exhibited the most substantial decline, with average metrics dropping by 12.20%, characterized by a narrower and elongated violin distribution. The removal of the DAG-GNN structure-learning module resulted in the second-largest decline (9.52%). In contrast, removing expert knowledge constraints or the GAT module led to relatively minor fluctuations. These results confirm that the significant synergy role between graph structure learning and the attention mechanism. The DAG-GNN module serves as the structural backbone, while knowledge constraints and GAT provide essential refinement for the model's predictive capability.

We further evaluated the robustness of the EDNN model under data sparsity by progressively reducing the training sample proportion from 80% to 20% (Fig. 10b). The ablation results indicate that even when the training data were reduced to 20%, all evaluation metrics remained above 0.7. Notably, the inferred DAG structures (Fig. 11) exhibited high stability, with the total number of connections remaining comparable (29, 29, 30, and 32, respectively). Meanwhile, the numbers of reversed, weak-effect, and erroneous edges showed certain fluctuations (8, 9, 12, and 15 in total), corresponding to proportions ranging from 54.84% to 72.41%. Under data ablation conditions, the predicted high-susceptibility zones slightly expanded (Supplementary-Fig. S2), indicating that the EDNN framework is capable of maintaining robust structural consistency and generalization ability even under limited training samples.

https://doi.org/10.5194/egusphere-2026-2637
Preprint. Discussion started: 20 May 2026

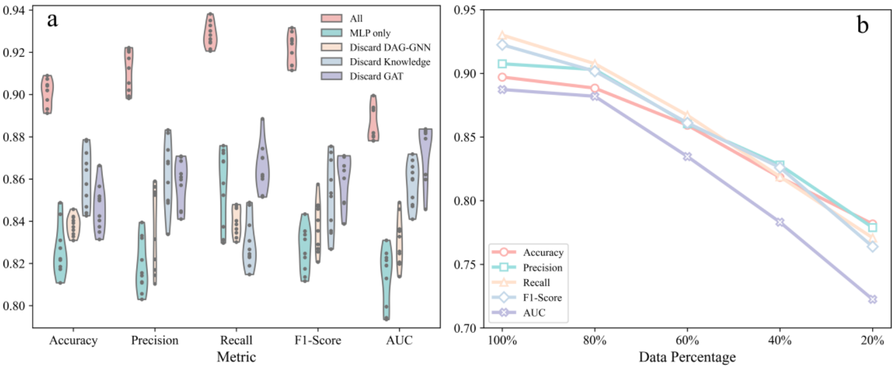

Figure 10: Ablation analysis. a. Module Ablation. All denotes the complete model; "MLP only" indicates retaining only the MLP for prediction; "Discard DAG-GNN" denotes the removal of the DAG-GNN model, other models are retained; "Discard Knowledge" represents the removal of expert knowledge constraints; "Discard GAT" indicates the omission of the graph attention mechanism. b. Data Ablation with training data reduced to 80%, 60%, 40%, and 20% of the original dataset analysis

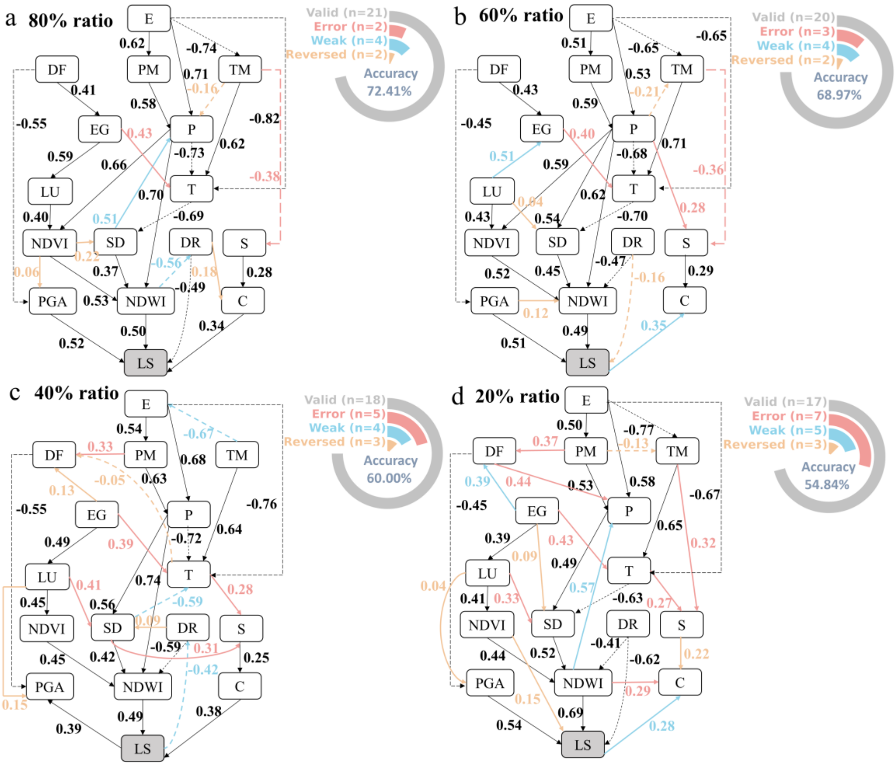

Figure 11: DAG structures under different data sampling ratios. Panels a–d show the DAGs obtained at sampling ratios of 80%, 60%, 40%, and 20%, respectively. Blue, yellow, red, and black edges denote implausible links requiring reversal, unreliable links to be removed, evidently implausible links to be eliminated, and reasonable links retained, respectively. The ring chart illustrates the numbers of correct and incorrect connections, along with the corresponding accuracy

https://doi.org/10.5194/egusphere-2026-2637
Preprint. Discussion started: 20 May 2026

5.2 Intervention analysis

Taking the representative dependency pathway Elevation (E) → Precipitation (P) → Temperature (T) → Snow Depth (SD) → Normalized Difference Water Index (NDWI) → Landslide occurrence (LS) as an example, we applied controlled perturbations to annual mean temperature (ΔT: −1.2 °C to 1.2 °C, step size 0.2 °C) and precipitation (ΔP: −120 mm to 120 mm, step size 20 mm) to evaluate how these variations influence the modeled landslide susceptibility pattern. Under temperature perturbations, the expansion of high susceptibility zones exhibits a generally linear trend. This suggests that temperature functions as a "slow-variable" driver, progressively preconditioning slope instability by changing long-term snowmelt dynamics, soil thermal regimes, and antecedent moisture states (Fig. 12a). In contrast, precipitation elicits a pronounced stepwise response, characterized by abrupt escalations in susceptibility once rainfall intensity exceeds critical thresholds (specifically around +50 mm). This threshold-dependent behavior identifies precipitation as a "fast-variable" trigger, triggering landslide occurrence through non-linear hydrological processes including rapid saturation excess and pore-water pressure (Fig. 12b).

These perturbation scenarios encompass conditions ranging from extreme cold–dry (ΔT = −1.2 °C, ΔP = −120 mm) to warm–wet (ΔT = 1.2 °C, ΔP = 120 mm). We found that the pathway importance increases as climatic variation shifts toward warm-wet conditions, indicating that the contribution of the selected pathway to the modeled susceptibility pattern increases overall. This is because temperature and precipitation perturbations propagate through the entire dependency pathway by jointly regulating snow accumulation–melt processes, soil moisture recharge, and surface hydrological connectivity. These coupled effects amplify downstream NDWI responses and ultimately reinforce the sensitivity of the susceptibility pattern to climatic forcing. Under extreme warm–wet conditions, causal pathway importance rises from 0.504 to 0.615, and the VH+H area proportion expands from 6.02% to 26.99%, mainly distributed in Zhaosu, Tekes, Xinyuan, and Nilka counties (Fig. 13), where the predicted area is consistent with Li et al. (2025).

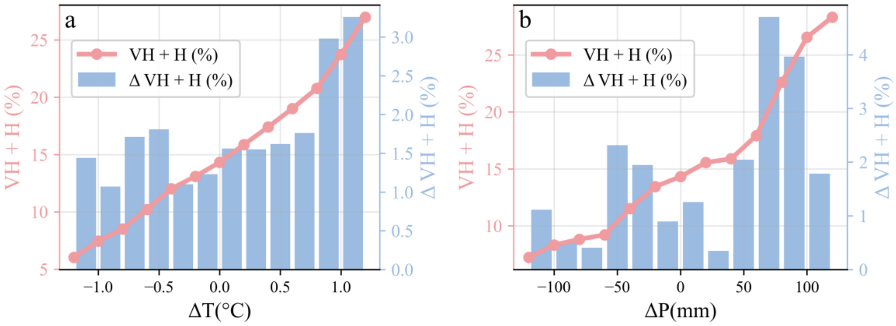

Figure 12: Illustrates the responses of the areal proportion of very high–high susceptibility zones (VH+H %) and the corresponding differences between adjacent intervals (ΔVH+H %) under different perturbation levels of (a) annual mean temperature and (b) annual mean precipitation (ΔT/ΔP)

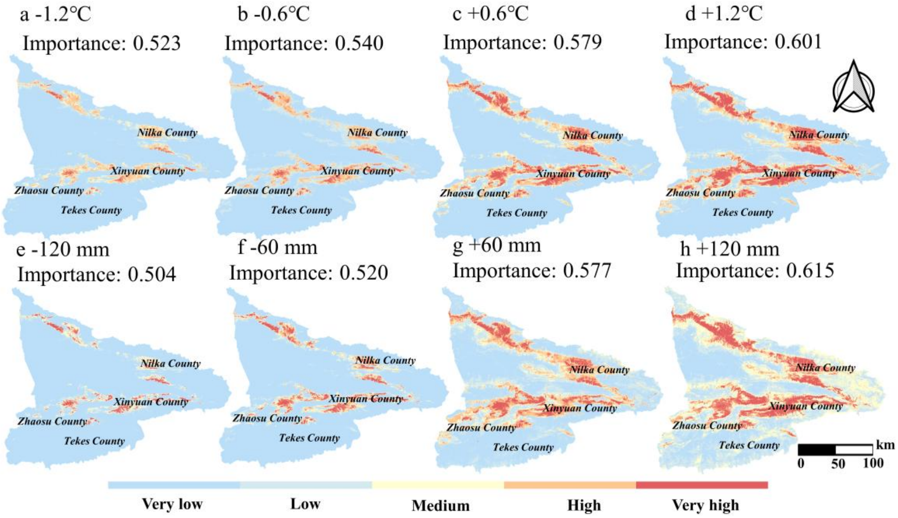

Figure 13: Landslide susceptibility maps corresponding to the "E → P → T → SD → NDWI → LS" dependency pathway under different temperature and precipitation change scenarios. Panels a–d show the landslide susceptibility results under four levels of temperature variation with an increment of 0.6 °C, while panels e–h show the landslide susceptibility results under four levels of precipitation variation with an increment of 60 mm (the baseline scenario is omitted). The importance of the corresponding dependency pathway for each result is also presented

5.3 Interpretation of dependency pathways

Pathway analysis identifies 14 dominant pathways, revealing that landslide formation is driven by the coupled effects of multi-pathway causal propagation. We found three categories factors impact landslides development: predisposing setting conditions (e.g., elevation, engineering geological lithology, distance to faults, slope, and curvature), mediating environmental factors (e.g., precipitation, temperature, land

https://doi.org/10.5194/egusphere-2026-2637
Preprint. Discussion started: 20 May 2026

use, NDVI, snow depth, and distance to rivers), and proximal variables (e.g., PGA and NDWI) (Fig. 14). Analysis based on the extracted dependency pathways (Table 3) indicates that predisposing factors define the static boundary conditions for landslide occurrence; their absence or specific combinations can fundamentally alter the spatial distribution pattern of landslides at the regional scale. Mediating environmental factors act as linking variables by regulating the stress state of slopes. Once hydrodynamic conditions or external loading exceed the slope-bearing capacity, these mediators create a critical state that makes slopes susceptible to failure under proximate factors. For example, in the mid–high mountainous areas of Nilka County, the elevation-driven chain (E → P → T → SD → NDWI → LS) dominates snowmelt-induced landslides. This pattern may reflect the combined association of topographic uplift with precipitation concentration, rising temperatures with enhanced snowmelt infiltration, and increased moisture with weakened vertical loess joints, which together correspond to higher regional-scale slope instability (Jin et al., 2024). In contrast, near the Kashi River fault zone, the tectonically driven chain (DF → PGA → LS) dominates, where historical strong earthquakes have generated clusters of coseismic landslides distributed along faults, highlighting the controlling effect of tectonic dynamics (Yin et al., 2003). Such hierarchical coupling leads to spatially heterogeneous instability patterns governed by different dependency pathways.

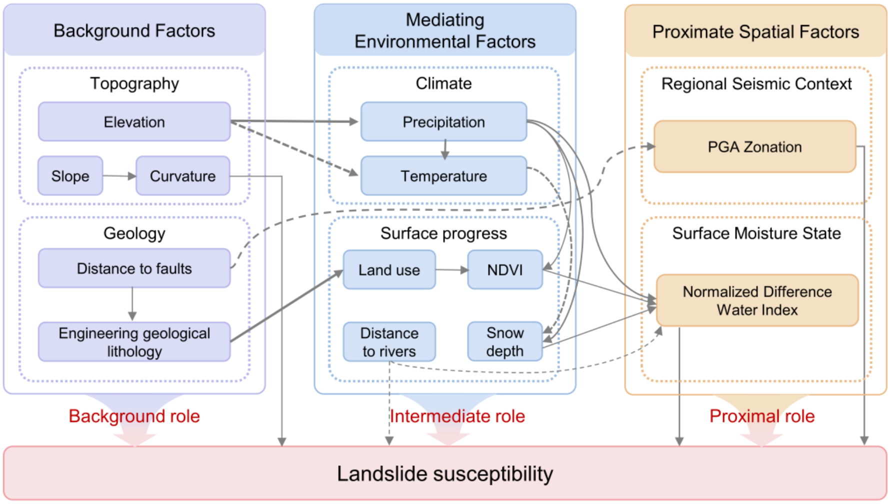

Figure 14: Hierarchical organization of susceptibility-related variables identified by our DAG-guided neural network

The counterintuitive dependency pathway "DF → EG → LU → NDVI → NDWI → LS" indicates that faults do not control landslides susceptibility solely through fractured zones. Instead, faults can also influence lithology, shape long-term stable micro-geomorphic units, and subsequently guide human land-use (LU) choices. Ultimately, by regulating vegetation cover (NDVI) and soil moisture (NDWI) through coupled "geological–ecological–hydrological" processes, faults create a landslide-prone environment that facilitates indirectly influence landslides susceptibility.

Another notable finding from the DAG structure is the pivotal role of NDWI (Normalized Difference Water Index) as a proximate spatial factor. Traditional deep learning methods often obscure this link by focusing solely on precipitation data for early warning (Segoni et al., 2025; Xie et al., 2025). However, our DAG-guided framework explicitly captures the "Precipitation → NDWI → Landslide" chain. This provides valuable insight for early warning in future: monitoring hydrological response indexes (like NDWI) may be more effective than monitoring rainfall thresholds. This finding offers precise guidance for refined regional disaster prevention, shifting focus from meteorological early warning to hydrological surface response monitoring.

Despite these advancements, the proposed approach faces challenges. One concern is latent confounders derived from low-quality data. This can be an artefact of the learned pathways. An example can be shown as "Slope → Landslide" (S→C→LS) might underscore unobserved intermediate variables (e.g., micro-structure changes or weathering degree of slopes). Second, the acyclic nature of DAGs limits the representation of feedback loops (Suzuki et al., 2020). Landslide evolution often involves bidirectional interactions (e.g., deformation inducing infiltration, which in turn accelerates deformation).

Future work should focus on two directions: (1) Data Fusion: Integrating multi-dimensional satellite observation data including InSAR, UAV and field surveys to capture missing intermediate nodes; (2) Exploring temporal-spatial graph-structure learning algorithms to model feedback loops and time-lagged effects. Although this study represents a simplified abstraction of the real landslide system, it successfully demonstrates the potential application of dependency networks in landslide assessment, which enable us some counterintuitive viewpoints as well as mitigation suggestions.

6 Conclusion

This study established an Explainable DAG-guided Neural Network (EDNN) framework for improving modeling interpretability of Landslide Susceptibility Assessment (LSA). We captured 14 robust dependency pathways and categorized four dominant pathway groups, including elevation–climate-driven, tectonic-controlled, hydrological driven, and Topographic dominated chains. Specifically, four representative pathways—E → P → NDWI → LS, E → P → T → SD → NDWI → LS, DF → PGA → LS, and S → C → LS—were selected for detailed analysis, as they dominate approximately 18.32%, 15.74%, 17.67%, and 16.76% of the high-susceptibility zones in the study area, respectively. We also show elucidate these influencing factors servers as background control, mediating regulator, and proximal roles during the landslides development progress. Ultimately, the most prominent pathways highlight the pivotal role of NDWI (Normalized Difference Water Index) as a sensitive hydrological factor for supporting more proactive disaster management strategies. This approach enhances the comprehensive understanding of landslide susceptibility pathways, overcoming the "black-box" limitations of conventional deep learning models.

Declaration of generative AI use

During the preparation of this work, the authors used Gemini for language editing. After using this tool, the authors reviewed and revised the content as necessary and take full responsibility for the content of the published article.

CRediT authorship contribution statement

Qingkai Meng: Conceptualization, Methodology, Writing – original draft, Writing – review & editing, Funding acquisition, Project administration. **Yong Dai:** Formal analysis, Data curation, Software, Writing – original draft. **Filippo Catani:** Supervision, Formal analysis, Writing – review & editing. **Shilong Chen:** Data curation, Writing – original draft. **Qiuhui Wang:** Data curation, Visualization. **Qing Li:** Data curation, Visualization. **Ying Peng:** Data curation, Visualization. **Han Wu:** Visualization. **Ying Meng:** Visualization.

Acknowledgments

This research was supported by the Third Xinjiang Scientific Expedition Program, grant number 2022xjkk0600; National Natural Science Foundation of China, grant number 42371091; the Young Talent Funding of the Chinese Academy of Sciences, grant number BR2024-01.

Data availability

The data sources have been disclosed in the manuscript, and the processed data are available upon reasonable request.

Declaration of competing interest

The authors have no competing interests to declare that are relevant to the content of this article.

References

Adadi, A., Berrada, M., 2018. Peeking inside the black-box: a survey on explainable artificial intelligence (XAI). IEEE Access. 6, 52138–52160. https://doi.org/10.1109/ACCESS.2018.2870052

Ailhamu, A., 2022. Characteristics of groundwater quality and its formation mechanism in the plain area of Ili River basin. Dissertation, Xinjiang Agricultural University (in Chinese).

Ali, S., Abuhmed, T., El-Sappagh, S., et al., 2023. Explainable Artificial Intelligence (XAI): What we know and what is left to attain Trustworthy Artificial Intelligence. Inf. Fusion. 99, 101805. https://doi.org/10.1016/j.inffus.2023.101805

Alvioli, M., Loche, M., Jacobs, L., et al., 2024. A benchmark dataset and workflow for landslide susceptibility zonation. Earth Sci. Rev. 258, 104927. https://doi.org/10.1016/j.earscirev.2024.104927

Bello, K., Aragam, B., Ravikumar, P., 2022. Dagma: Learning dags via m-matrices and a log-determinant acyclicity characterization. Adv. Neural Inf. Process. Syst. 35, 8226–8239.

Bhattarai, T.R., Bhandary, N.P., Pandit, K., 2026. Prediction of Coseismic Landslides by Explainable Machine Learning Methods. GeoHazards. 7, 7. https://doi.org/10.3390/geohazards7010007

Cruden, D.M., Varnes, D.J., 1996. Landslide types and processes. In: Turner, A.K., Schuster, R.L. (Eds.), Landslides: Investigation and Mitigation. Special Report 247. Transportation Research Board, Washington, D.C., pp. 36–75.

Caleca, F., Confuorto, P., Raspini, F., et al., 2025. Modelling landslide susceptibility through a glass-box machine learning. In: EGU General Assembly Conference Abstracts, pp. EGU25-5730. 10.5194/egusphere-egu25-5730

Camps-Valls, G., Fernández-Torres, M.Á., Cohrs, K.H., et al., 2025. Artificial intelligence for modeling and understanding extreme weather and climate events. Nat. Commun. 16, 1919. https://doi.org/10.1038/s41467-025-56573-8

Castro-Venegas, F., Jaque, E., Quezada, J., Palma, J.L., Fernandez, A., 2025. Multi-source landslide inventories for susceptibility assessment: a case study in the Concepción Metropolitan Area, Chile. Front. Earth Sci. 13, 1534295. https://doi.org/10.3389/feart.2025.1534295

Chen, S., Meng, Q., Dai, Y., et al., 2025. Geological disaster hazard assessment and prediction in the Ili River Basin based on CMIP6 future scenarios. Arid Land Geogr. 48, 599–611. https://doi.org/10.12118/j.issn.1000-6060.2024.520 (in Chinese).

Chen, W., Zhao, X., Shahabi, H., Shirzadi, A., Khosravi, K., Chai, H., Ahmad, B.B., 2021. GIS-based comparative study of Bayes network, Hoeffding tree and logistic model tree for landslide susceptibility modeling. Catena. 203, 105344. https://doi.org/10.1016/j.catena.2021.105344

Dai, Y., Meng, Q., Chen, S., et al., 2024. Landslide hazard evaluation based on BPNN-SHAP model: A case study of the Yili River Basin, Xinjiang Province. Sediment Geol. Tethyan Geol. 44, 534–546. https://doi.org/10.19826/j.cnki.1009-3850.2024.07006 (in Chinese).

Digitale, J.C., Martin, J.N., Glymour, M.M., 2022. Tutorial on directed acyclic graphs. J. Clin. Epidemiol. 142, 264–267. https://doi.org/10.1016/j.jclinepi.2021.08.001

Gao, X., Wang, B., Dai, W., Liu, Y., 2025. A landslide susceptibility assessment method using SBAS-InSAR to optimize Bayesian network. Front. Environ. Sci. 13, 1522949. https://doi.org/10.3389/fenvs.2025.1522949

Guzzetti, F., Mondini, A.C., Cardinali, M., et al., 2012. Landslide inventory maps: New tools for an old problem. Earth Sci. Rev. 112, 42–66. https://doi.org/10.1016/j.earscirev.2012.02.001

Havenstrite, R., et al., 2015. Tien Shan Geohazards Database: Earthquakes and landslides. Geomorphol. 249, 104–121. https://doi.org/10.1016/j.geomorph.2015.03.020

Hu, Y., Zhang, Z., Lin, S., 2023. Evaluation of Landslide Susceptibility in Ili Valley, Xinjiang Based on the Coupling of WOE Model and Logistic Regression. Eng. Geol. 31, 1350–1363. https://doi.org/10.13544/j.cnki.jeg.2023-0128 (in Chinese).

Hussain, M.A., Chen, Z., Zhou, Y., et al., 2025. Landslide susceptibility mapping using artificial intelligence models: a case study in the Himalayas. Landslides. 22, 2089–2103. https://doi.org/10.1007/s10346-025-02466-2

Jin, C., Wang, B., Cheng, T.F., et al., 2024. How much we know about precipitation climatology over Tianshan Mountains—the Central Asian water tower. npj Clim. Atmos. Sci. 7, 21. https://doi.org/10.1038/s41612-024-00572-x

Lee, S., Roh, M., Jo, H.W., et al., 2025. Machine learning-based rainfall-induced landslide susceptibility model and short-term early warning assessment in South Korea. Landslides. 22, 2809–2827. https://doi.org/10.1007/s10346-025-02513-y

Li, X., Liu, J., Zhang, Z., et al., 2025. Geological Disaster Risk Assessment Under Extreme Precipitation Conditions in the Ili River Basin. ISPRS Int. J. Geo-Inf. 14, 346. https://doi.org/10.3390/ijgi14090346

Li, Y., Fu, B., Yin, Y., et al., 2024. Review on the artificial intelligence-based methods in landslide detection and susceptibility assessment: Current progress and future directions. Intelligent Geoengineering 1, 1–18. https://doi.org/10.1016/j.ige.2024.10.003

Li, Y., Yang, G., Ye, W., et al., 2023. Deterioration law and microscopic mechanism of hydraulic characteristics of undisturbed loess in Ili under freeze-thaw cycles. Eng. Geol. 41, 1234–1245. https://doi.org/10.12401/j.nwg.20220730 (in Chinese).

Liu, X., Di, X., 2021. TanhExp: A smooth activation function with high convergence speed for lightweight neural networks. IET Comput. Vis. 15, 136–150. https://doi.org/10.1049/cvi2.12020

Matougui, Z., Daksi, Y.M., Dib, M., Benabbas, C., 2025. Decoupling urban and non-urban landslides for susceptibility mapping in transitional landscapes: a case study from Southwestern Constantine, Algeria. Nat. Hazards Earth Syst. Sci. 25, 4629–4653. https://doi.org/10.5194/nhess-25-4629-2025

Nocentini, N., Rosi, A., Piciullo, L., Liu, Z., Segoni, S., Fanti, R., 2024. Regional-scale spatiotemporal landslide probability assessment through machine learning and potential applications for operational warning systems: a case study in Kvam (Norway). Landslides 21, 2369–2387. https://doi.org/10.1007/s10346-024-02287-9

Pearl, J., 2000. Causality: Models, Reasoning, and Inference. Cambridge University Press, Cambridge.

Pradhan, B., Dikshit, A., Lee, S., Kim, H., 2023. An explainable AI (XAI) model for landslide susceptibility modeling. Appl. Soft Comput. 142, 110324. https://doi.org/10.1016/j.asoc.2023.110324

Rahimikhameneh, L., Alvarez Reyna, A., Montgomery, J., O'Donnell, F., 2025. Usage of normalized soil moisture for improving the performance of rainfall thresholds for landslides along transportation corridors. EGUsphere. 2025, 1–28. https://doi.org/10.5194/egusphere-2025-3419

Segoni, S., Nocentini, N., Barbadori, F., Medici, C., Gatto, A., Rosi, A., Casagli, N., 2025. A novel prototype national-scale landslide nowcasting system for Italy combining rainfall thresholds and risk indicators. Landslides. 22, 1341–1366. https://doi.org/10.1007/s10346-024-02452-0

Shimizu, S., Hoyer, P.O., Hyvärinen, A., Kerminen, A., Jordan, M., 2006. A linear non-Gaussian acyclic model for causal discovery. J. Mach. Learn. Res. 7, 2003–2030.

Steger, S., Mair, V., Kofler, C., Pittore, M., Zebisch, M., Schneiderbauer, S., 2021. Correlation does not imply geomorphic causation in data-driven landslide susceptibility modelling–Benefits of exploring landslide data collection effects. Sci. Total Environ. 776, 145935. https://doi.org/10.1016/j.scitotenv.2021.145935

Suzuki, E., et al., 2020. Causal Diagrams: Pitfalls and Tips. J. Epidemiol. 30, 153–162. https://doi.org/10.2188/jea.JE20190097

Tao, K., Wang, L., Qian, X., 2016. Multi-factor constrained analysis method for geological hazard risk. Int. J. Eng. Technol. 8, 198–201. https://doi.org/10.7763/ijet.2016.v6.884

Utthasini, M., Ilampooranan, I., Singh, S.K., et al., 2025. Enhancing landslide susceptibility mapping in the Himalayas: geospatial and machine learning with explainable AI. Gondwana Res. 149, 262–290. https://doi.org/10.1016/j.gr.2025.08.003

Veličković, P., Cucurull, G., Casanova, A., Romero, A., Lio, P., Bengio, Y., 2017. Graph attention networks. arXiv preprint arXiv:1710.10903. https://doi.org/10.48550/arXiv.1710.10903

Xie, X., Du, J., Yin, K., Macciotta, R., Liu, S., Jiang, J., Yang, H., 2025. Slope-specific rainfall thresholds for regional landslide early warning systems. Eng. Geol. 355, 108249. https://doi.org/10.1016/j.enggeo.2025.108249

Xu, J.L., Liu, S.Y., Guo, W.Q., Zhang, Z., Wei, J.F., Feng, T., 2015. Glacial area changes in the Ili river catchment (Northeastern Tianshan) in Xinjiang, China, from the 1960s to 2009. Adv. Meteorol. 2015, 847257. https://doi.org/10.1155/2015/847257

Xu, Y., Lu, Z., Leshchinsky, B., 2022. Kinematics of irrigation-induced landslides in a Washington Desert: impacts of basal geometry. J. Geophys. Res. Earth Surf. 127, e2021JF006355. https://doi.org/10.1029/2021JF006355

Yin, G., Jiang, J., Zhang, Y., 2003. Research on Kashi River Fault in Yili Xinjiang and its activity. Internal. Seismol. 17, 109–116. https://doi.org/10.16256/j.issn.1001-8956.2003.02.003 (in Chinese).

Youssef, K., Shao, K., Moon, S., et al., 2023. Landslide susceptibility modeling by interpretable neural network. Commun. Earth Environ. 4, 162. https://doi.org/10.1038/s43247-023-00806-5

Yu, Y., Chen, J., Gao, T., Yu, M., 2019. DAG-GNN: DAG structure learning with graph neural networks. In: Int. Conf. Mach. Learn., vol. 97, PMLR, pp. 7154–7163.

Zhang, M., Fu, X., Liu, S., Zhang, C., 2025. Integrating Remote Sensing and Machine Learning for Actionable Flood Risk Assessment: Multi-Scenario Projection in the Ili River Basin in China Under Climate Change. Remote Sens. 17, 1189. https://doi.org/10.3390/rs17071189

Zhao, Y., Jia, J., 2025. DAGSLAM: causal Bayesian network structure learning of mixed type data and its application in identifying disease risk factors. BMC Med. Res. Methodol. 25, 154. https://doi.org/10.1186/s12874-025-02582-6

Zheng, X., Aragam, B., Ravikumar, P.K., Xing, E.P., 2018. Dags with no tears: Continuous optimization for structure learning. Adv. Neural Inf. Process. Syst. 31.

Zhou, S., Li, J., Zhang, J., Xu, Z., Lu, X., 2024. Exploring Bayesian network model with noise filtering for rainfall-induced landslide susceptibility assessment in Fujian, China. Front. Earth Sci. 12, 1444882. https://doi.org/10.3389/feart.2024.1444882

Zhou, X., Xing, Y., 2025. Spatial consistency assessment and landslide susceptibility prediction optimization. Front. Earth Sci. 13, 1702688. https://doi.org/10.3389/feart.2025.1702688